NANO · MICRO small
www.small-journal.com

Fracture Resistant $CrSi_2$-Doped Silicon Nanoparticle Anodes for Fast-Charge Lithium–Ion Batteries

Weiqun Li, Chucheng Luo, Jimin Fu, Juan Yang, Xiangyang Zhou, Jingjing Tang, and B. Layla Mehdi**

Lithium–ion batteries (LIBs) has been developed over the last three decades. Increased amount of silicon (Si) is added into graphite anode to increase the energy density of LIBs. However, the amount of Si is limited, due to its structural instability and poor electronic conductivity so a novel approach is needed to overcome these issues. In this work, the synthesized chromium silicide ($CrSi_2$) doped Si nanoparticle anode material achieves an initial capacity of 1729.3 mAh g^{-1} at 0.2C and retains 1085 mAh g^{-1} after 500 cycles. The new anode also shows fast charge capability due to the enhanced electronic conductivity provided by $CrSi_2$ dopant, delivering a capacity of 815.9 mAh g^{-1} at 1C after 1000 cycles with a capacity degradation rate of <0.05% per cycle. An in situ transmission electron microscopy is used to study the structural stability of the $CrSi_2$-doped Si, indicating that the high control of $CrSi_2$ dopant prevents the fracture of Si during lithiation and results in long cycle life. Molecular dynamics simulation shows that $CrSi_2$ doping optimizes the crack propagation path and dissipates the fracture energy. In this work a comprehensive information is provided to study the function of metal ion doping in electrode materials.

1. Introduction

Lithium–ion batteries (LIBs) have become one of the most important energy storage systems. However, graphite anode, with theoretical capacity of only 372 mAh g^{-1}, limits the energy density of LIBs. To increase the overall capacity of anode, silicon (Si) has been added into graphite anode due to its high theoretical capacity (4200 mAh g^{-1}).[1–4] However, two main issues hinder the practical and scale-up application of Si-based anode: structural instability[5,6] and low electronic conductivity.[7,8]

The structural instability stems from the fracture of Si electrode materials, which is induced by the large volume change (over 300%) during electrochemical cycling.[6,9] The solid electrolyte interface (SEI) forming on Si surface can be cracked after the Si electrode is fractured, leading to the direct contact between the electrolyte and newly exposed Si surface.[10] Such contact results in the formation of new SEI layer, consumption of active Si materials and electrolyte, and failure of LIB. Therefore, different design methods have been applied to alleviate and prevent the fracture of Si anode, such as nanomaterial design,[11–14] coating strategy,[15–18] electrolyte, and additive optimization,[19,20] geometrical electrode design,[21,22] etc. For example, yolk-shell hierarchical nanostructured carbon-coated Si

---

W. Li, B. L. Mehdi
Department of Mechanical
Materials and Aerospace Engineering
University of Liverpool
Liverpool L69 3GH, UK
E-mail: b.l.mehdi@liverpool.ac.uk

W. Li, B. L. Mehdi
The Faraday Institution
Harwell Campus
Didcot OX11 0RA, UK

C. Luo, J. Yang, X. Zhou, J. Tang
School of Metallurgy and Environment
Central South University
Changsha, Hunan 410083, China
E-mail: tangjj@csu.edu.cn

C. Luo
College of Chemistry and Materials Engineering
Hunan University of Arts and Science
Changde, Hunan 415000, China

J. Fu
Research Institute for Intelligent Wearable Systems
School of Fashion and Textiles
Hong Kong Polytechnic University
Hong Kong SAR 999077, P. R. China

B. L. Mehdi
Albert Crewe Centre for Electron Microscopy
University of Liverpool
Liverpool L69 3GL, UK

The ORCID identification number(s) for the author(s) of this article can be found under https://doi.org/10.1002/smll.202308304

DOI: 10.1002/smll.202308304

anode materials were synthesized to accommodate the volume change of Si during electrochemical cycling, leading to high capacity, and long cycle life.[13,23] In addition to nanoparticle (NP) materials, 2D porous Si nanosheet anode was designed to enhance the lithiation and delithiation processes and therefore increase the mass capacity.[14] By using effective electrolyte additive, such as a combination of vinylene carbonate, fluoroethylene carbonate (FEC), and lithium difluorooxalatoborate, the SEI composition and structure were optimized, leading to higher cycling efficiency and capacity retention of Si-based anode materials.[19] The delamination problem between Si materials and copper (Cu) current collector, caused by the dramatic volume change of Si, was mitigated by optimally designed 3D current collector[21] and graded Si electrode.[22] The above methods, by mainly changing the extrinsic environment of Si-based anode materials, have been shown to effectively alleviate the structural instability problem.

The second issue regarding the low electronic conductivity arises from the intrinsic electronic structure of Si, which largely limits the charge rate of Si anode. To increase the electronic conductivity of Si anode, some methods have been proposed and studied, such as conductive network design,[24–26] doping,[27–31] etc. For example, carbon nanotube[24,25] and graphene,[26] as electronic conductivity enhancers, have been widely used to create a high-conductivity carbon network and increase the charge rate for Si-based anode materials. In recent years, doping strategies have been adopted to increase the electronic conductivity of Si-based anode materials. For example, the 5-sulfoisophthalic acid doping in polyaniline coating served as a conductive matrix by improving electrical contact and adhesive force for Si NP anode materials.[27] Furthermore, phosphorus doping,[28] tungsten (W) doping,[29] chromium or molybdenum dopings,[30] and boron doping[31] have been shown to facilitate the electron transport and electrochemical reaction activity, leading to better rate performance for Si anode. Nevertheless, most of these works were mainly based on electrochemical measurements, and it is still unclear how doping materials increase the electronic conductivity and extend the cycle life for Si-based anode materials at the nanoscale in real time.

In the last ten years, in situ TEM has been used to study battery materials due to its high spatial and temporal resolutions.[9,32–37] For example, in situ TEM was first used to characterize the lithiation process in the tin dioxide nanowire anode.[32] The atomic level phase transformation and volume change were observed and analyzed during electrochemical cycling processes. The in situ TEM was subsequently applied to Si-based anode materials. A two-phase reaction mechanism was observed for crystalline Si NP materials during in situ TEM lithiation.[33] In addition, critical sizes, below that no crack occurs, were observed for both crystalline[6] and amorphous[9] Si NPs. The effect of carbon matrix and coating on Si anode was also studied through in situ TEM, providing the optimization design strategies to prevent the fracture of Si NPs.[16,17,34] Therefore, in situ TEM has been regarded as an effective experimental approach to study the nanoscale morphological, structural, and compositional changes of new Si-based anode materials in real time.

In this work, we synthesized the $CrSi_2$-doped Si (Si/Cr) NP anode materials and measured the electrochemical performance, including cyclic voltammetry (CV), galvanostatic charge/discharge, rate performance, and electrochemical impedance spectroscopy (EIS). We conducted in situ TEM characterization, in which the fracture occurrence, phase transformation, and volume change were directly observed during lithiation. To explain how the $CrSi_2$ doping improved the structural stability and electronic conductivity of the Si-based anodes, molecular dynamics (MD) simulation was conducted, showing the increased fracture toughness by the $CrSi_2$ nanocrystals in the Si matrix. Our work shows the $CrSi_2$ doping effectively improves the charge rate and cycling performance of Si/Cr NP anode by increasing the electronic conductivity and maintaining the structural integrity during electrochemical cycling.

2. Results and Discussion

2.1. Materials Characterization

TEM was used to characterize the morphologies and structures of p-Si, Si-8%Cr, and Si-18%Cr, as shown in **Figure** 1a–f. The NPs have sphere-like morphologies, and the sizes of the NPs range from tens to hundreds of nanometres. The p-Si NPs show the (111) lattice plane with d-spacing of 3.12 Å, which can be seen from the HRTEM image in Figure 1d. The $CrSi_2$ nanocrystals are either attached on or embedded in the Si-8%Cr and Si-18%Cr materials, as shown in Figure 1e,f, respectively. The $CrSi_2$ nanocrystals, showing (111) lattice planes with d-spacing of 2.10 Å, can be seen in Figure 1e,f, while Si (111) lattice planes are distributed in the surrounding area. Energy dispersive X-ray (EDS) mapping was conducted to image the elemental distribution for Si-8%Cr and Si-18%Cr in Figure S1 (Supporting Information). In both cases, the doped $CrSi_2$ (Figure S1c,f, Supporting Information) is widespread in the Si matrix (Figure S1b,e, Supporting Information). Figure 1g shows the volume change of the p-Si and Si/Cr NPs during lithiation processes, in which the p-Si NP could be cracked while the Si/Cr NP tends to remain structural integrity.

The structural and compositional properties of the p-Si and Si/Cr NPs were characterized by X-ray diffraction (XRD) analysis, as shown in **Figure** 2. Compared with the standard spectrum of Si (JCPDS No. 27–1402), additional peaks can be observed in the XRD patterns of Si/Cr NPs with different doping percentages, which coincide with the crystal form of $CrSi_2$ (JCPDS No. 65–9705). By increasing the Cr content from 8% to 18%, the diffraction peak intensity of $CrSi_2$ is increased. The XRD results indicate that the Si/Cr NPs were successfully synthesized with the doped Cr present in the form of $CrSi_2$ crystals. Based on ICP test results, the ratio of Cr in Si-8%Cr, Si-12%Cr, Si-16%Cr, and Si-18%Cr are measured to be 8.2%, 15%, 20%, and 22.5%, respectively.

2.2. Electrochemical Performance

The CV tests of p-Si and Si-8%Cr anodes were performed at a scan rate of 0.1 mV s^{-1} from 0.01 and 1.2 V (**Figure** 3a,b). The CV curves of the two samples exhibit similar characteristics with one cathodic peak and two anodic peaks. The peak intensity of the Si-8%Cr sample is higher than that of p-Si, suggesting the higher capacity of Si-8%Cr. During the first cycle, the wide peak ranging from 0.4 to 0.7 V is ascribed to the formation of SEI film. The apparent cathodic peaks at 0.2 V and anodic peaks at 0.34 – 0.52 V are associated with the reversible lithiation from Si to Li_xSi

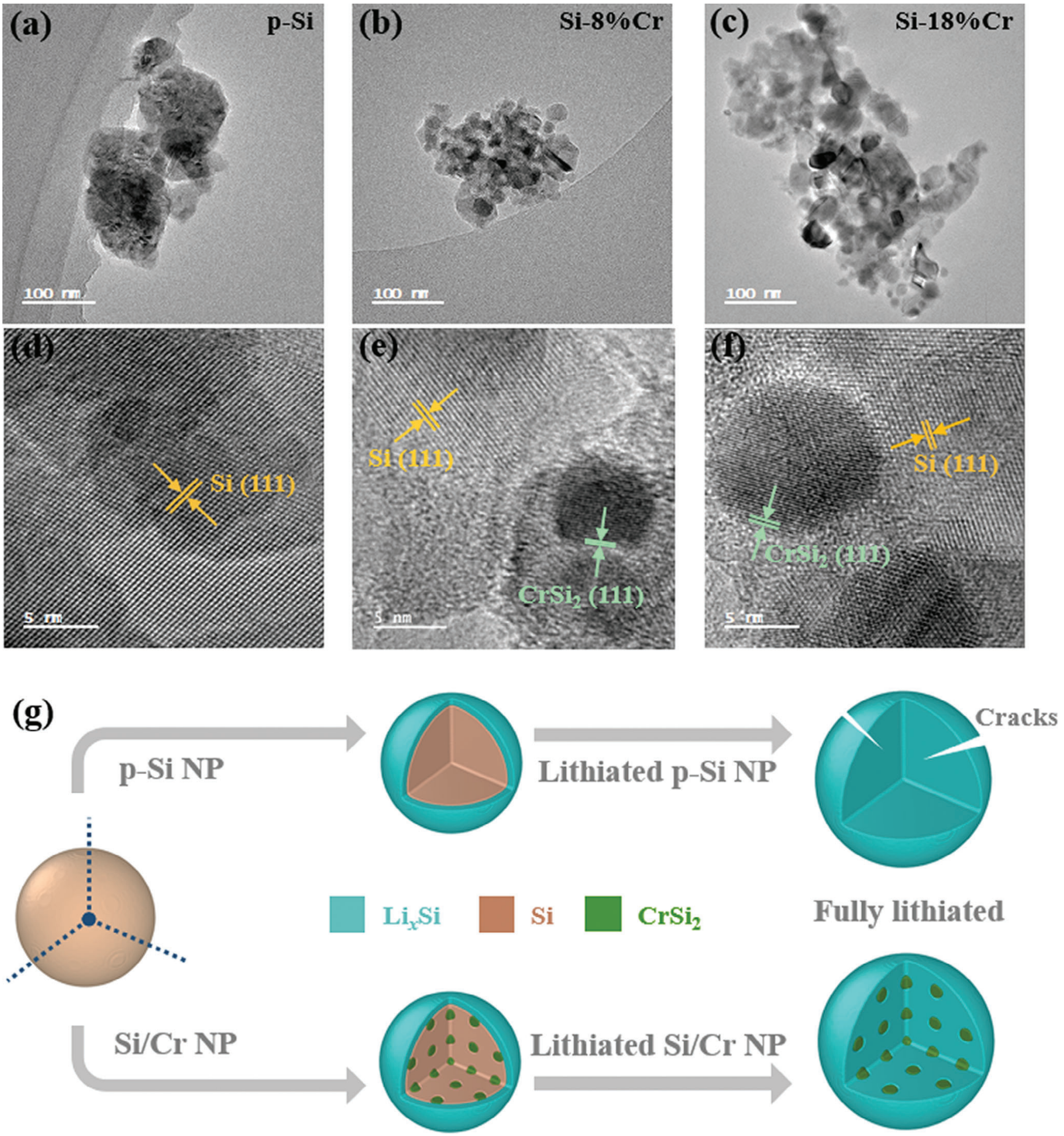

Figure 1. HRTEM images of a, d) p-Si, b, e) Si-8%Cr, and c, f) Si-18%Cr nanoparticles. g) Schematic showing the lithiation processes of p-Si and Si/Cr nanoparticles.

and delithiation from Li$_x$Si to Si, respectively. In the following cycles, the gradually reinforced peaks indicate that the electrode is gradually wetted by electrolyte, which was resulted by gradually increased amount of lithiated Si. To investigate the effect of CrSi$_2$ on the electrochemical properties of Si anode, the CV curves of the pure CrSi$_2$ anode in the initial 5 cycles between 0.01 and 1.2 V is presented in Figure S2 (Supporting Information). Compared with the p-Si and Si-8%Cr anodes, there is no obvious cathodic or anodic peak, indicating the low electrochemical reactivity of CrSi$_2$, which matches well with the in situ TEM lithiation results (see Section 3).

The charge–discharge profiles of p-Si and Si-8%Cr anodes are recorded at 0.2C (1C = 4200 mA g^{-1}) in the voltage range of 0.01 and 1.2 V, as shown in Figure 3c,d. The plateau below 0.1 V

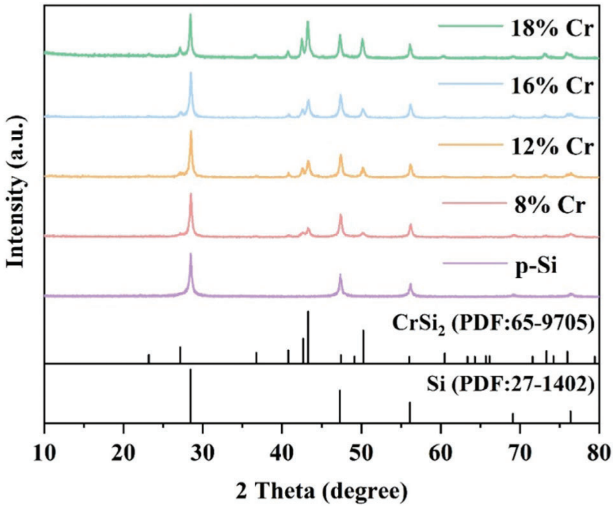

Figure 2. XRD patterns of p-Si, Si-8%Cr, Si-12%Cr, Si-16%Cr, and Si-18%Cr nanoparticles.

in the initial discharge curve is caused by the lithiation process of crystalline Si. During the following charge process, voltage plateau near 0.4 V is related to the delithiation process from amorphous Li$_x$Si to Si. Besides, the initial discharge capacities of p-Si and Si-8%Cr anodes are 2277.1 and 2772.7 mAh g^{-1}, respectively, indicating that the CrSi$_2$ doping improves the specific capacity of Si. Furthermore, the Si-8%Cr anode exhibits a more stable polarization potential between discharge and charge plateaus from the 1st to 500th cycles, indicating the stability of the electrode.

Figure 4a shows the cycling performance of all samples at 0.05C in the initial 3 cycles for activation and at 0.2C in the following cycles. After cycled at 0.05C for activation, the initial charge capacities of Si-8%Cr, Si-12%Cr, Si-16%Cr, Si-18%Cr, and p-Si anodes at 0.2C are 1729.3 mAh g^{-1}, 1644.4 mAh g^{-1}, 1210.2 mAh g^{-1}, 959.4 mAh g^{-1}, and 1399.1 mAh g^{-1}, respectively. After 500 cycles, they retain 1085 mAh g^{-1}, 1037.7 mAh g^{-1}, 810.7 mAh g^{-1}, 475.3 mAh g^{-1} and 161.3 mAh g^{-1}, corresponding to the capacity retention rates of 62.7%, 63.1%, 67%, 49.5%, and 11.5%, respectively. It is noticed that the Si/Cr anodes with 8–16% Cr doping exhibit superior cyclic stability, because of the synergistic effect of their enhanced electronic conductivity and structural stability. Nevertheless, the Si-18%Cr electrode delivers the lowest initial charge capacity due to the high amount of CrSi$_2$ in the materials, which leads to the incomplete lithiation of Si/Cr anode materials. During the activation processes under 0.05C, the initial reversible capacities of Si-8%Cr, Si-12%Cr, Si-16%Cr, Si-18%Cr, and p-Si are 2092.3 mAh g^{-1}, 1955.5 mAh g^{-1}, 1363.6 mAh g^{-1}, 1137.6 mAh g^{-1}, and 1574.1 mAh g^{-1}, corresponding to the initial coulombic efficiencies (ICE) of 75.46%, 74.86%, 71.65%, 68.09%, and 69.13%, respectively. It can be found that the ICE of Si/Cr electrodes decreases with the increase of Cr concentration, and the Si-18%Cr electrode delivers the lowest ICE, which could be related to its low electrochemical reactivity. To investigate the effect of CrSi$_2$ on the cycling performance of Si anode, the pure CrSi$_2$ anode, and the mechanically mixed anode of CrSi$_2$ and Si (p-Si@CrSi$_2$, with same Cr doping as Si-8%Cr) are cycled at 0.2C for 500 cycles after being activated at 0.05C for the initial 3 cycles (Figure S3, Supporting Information). After repeated cycling, p-Si@CrSi$_2$ anode revealed a similar trend of capacity degradation as p-Si but with a lower capacity. In comparison, the pure CrSi$_2$ anode delivered a very low initial charge capacity of 122 mAh g^{-1}, corresponding to an ICE of 32.11%, which is comparable with the data in reference.[30]

Moreover, the Si-8%Cr anode delivers the best rate capability at various current densities (Figure 4b). The reversible capacities of Si-8%Cr anode at 0.05, 0.1, 0.2, 0.4, 0.8, 1.6, and 2C are ≈2081.7, 1956.7, 1796.4, 1460.9, 1176.2, 777.0, and 582.3 mAh g^{-1}, respectively. When the current recovers to 0.05C, the reversible capacity of the Si-8%Cr returns to 1960.6 mAh g^{-1} and remains steadily in the following cycles. It should be noted that the Si-12%Cr electrode exhibits the same level of cyclability compared with Si-8%Cr at 2C, indicating the vital role of CrSi$_2$ in enhancing the cycling stability. The increased electronic conductivity can be confirmed by the EIS data in Figure S4 (Supporting Information), indicating the reduced impedance by CrSi$_2$ doping.

Based on the above electrochemical experimental results, the excellent long-term cycling performance of the Si/Cr electrodes is expected. After initial 3 activation cycling at 0.21 A g^{-1}, the Si-8%Cr, Si-18%Cr, and p-Si electrodes were tested with a higher current density (1C). As shown in Figure 4c, the capacity of Si-8%Cr decreases briefly after the initial activation cycles due to the ICE and then climbs gradually during the following 30 cycles, which can be ascribed to the rapid rearrangement of active materials under high current density and formation of a gradually stabilized SEI. Noteworthily, the Si-8%Cr electrode delivers an excellent capacity of 815.9 mAh g^{-1} over 1000 cycles, with a capacity degradation rate of 0.0469% per cycle from the 4th cycle, which indicates the effectiveness of embedded CrSi$_2$. In contrast, the Si-18%Cr anode exhibits a very low reversible capacity of ≈734.3 mAh g^{-1} after 3 activation cycles due to the low-electrochemical reactivity of CrSi$_2$. Furthermore, although the p-Si anode delivers a higher initial reversible capacity than the Si-18%Cr one, its capacity suffers a rapid degradation during cycling because of the structural instability and poor electronic conductivity, and the corresponding coulombic efficiencies (CE) of Si-8%Cr, Si-18%Cr, and p-Si are shown in Supplementary Material (Figure S5, Supporting Information).

2.3. In Situ TEM Lithiation

To explain how CrSi$_2$ doping improves the cycle life of Si NP anode at nanoscale, in situ TEM lithiation was conducted for the p-Si, Si-8%Cr, and Si-18%Cr NP anodes. **Figure** 5a shows the schematic of the in situ TEM setup of an open cell, in which the NPs are attached on the half-moon Cu grid, and the Li metal is scraped on the W needle. The time-resolved TEM images in Figure 5b–g show the lithiation process of the p-Si NPs, during that the Li diffuses from the outer Si layer into the inner Si core, leading to a volume expansion. An obvious interface can be seen between the lithiated Si shell and the pristine Si core in Figure 5c–g, which has been reported elsewhere.[6,16,33,34] From 0.8 s, a crack, indicated by the red arrow in Figure 5f,g, forms from the edge of the p-Si NP. Such crack is caused by the increased tensile stress in the lithiated Si shell exceeding its tensile

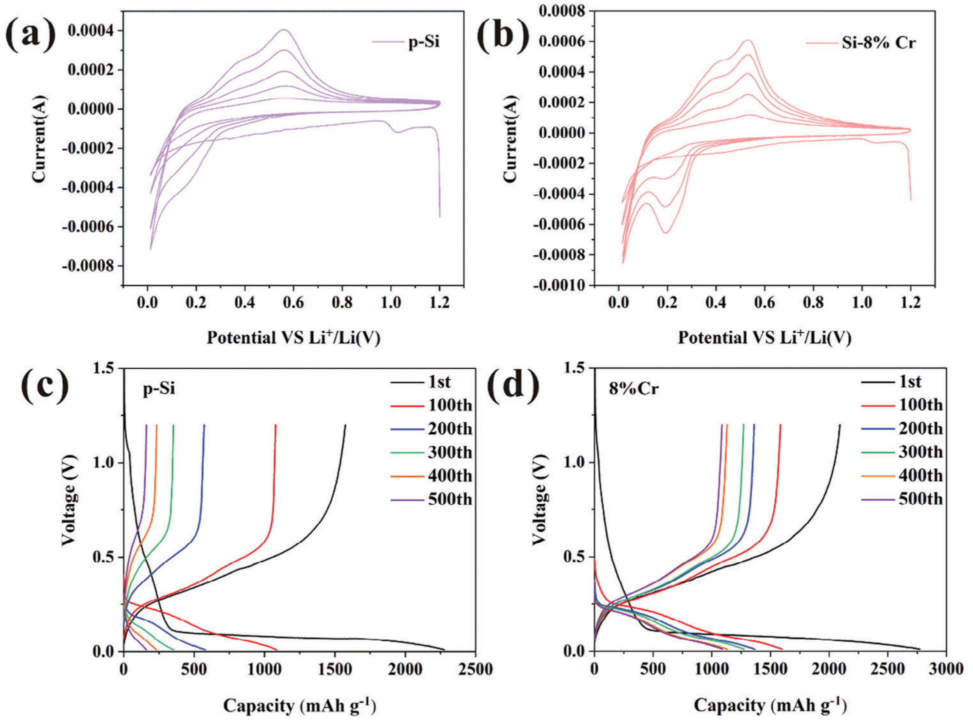

Figure 3. Cyclic voltammetry profiles of a) p-Si and b) Si-8%Cr anodes in the initial five cycles measured at a scanning rate of 0.2 mV s^{-1}. Discharge/charge profiles of c) p-Si and d) Si-8%Cr anodes from 1st to 500th cycle.

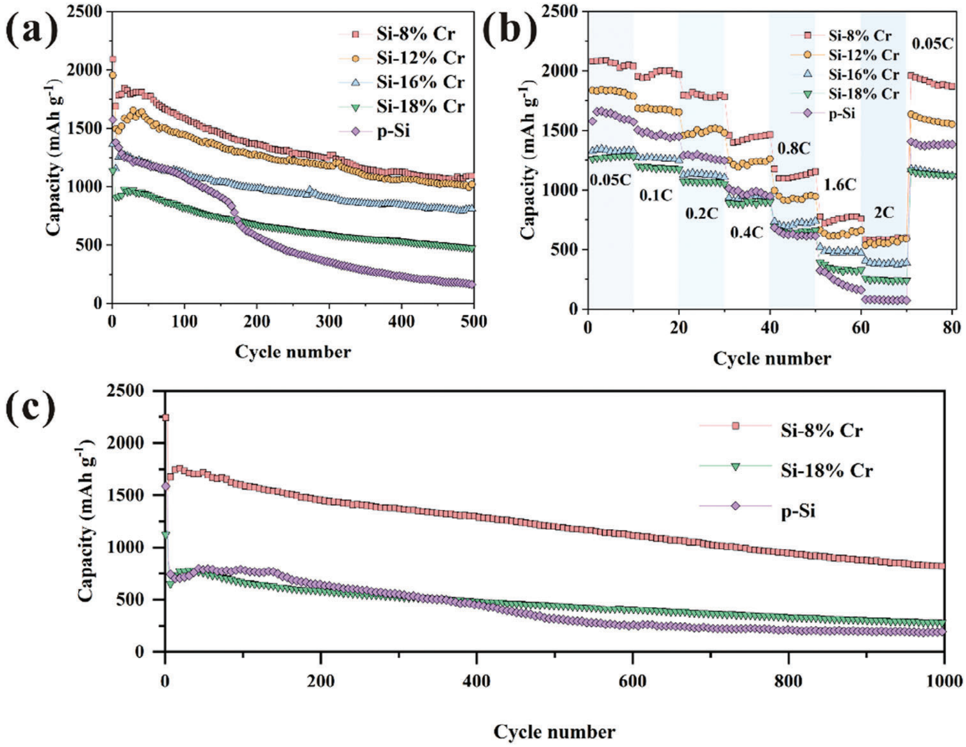

Figure 4. a) Cyclic performance of Si-8%Cr, Si-12%Cr, Si-16%Cr, Si-18%Cr, and p-Si anodes at 0.2C, b) corresponding rate performance at varying rates from 0.05 to 2C, and c) long-term cycling performance of Si-8%Cr, Si-18%Cr, and p-Si anodes at 1C.

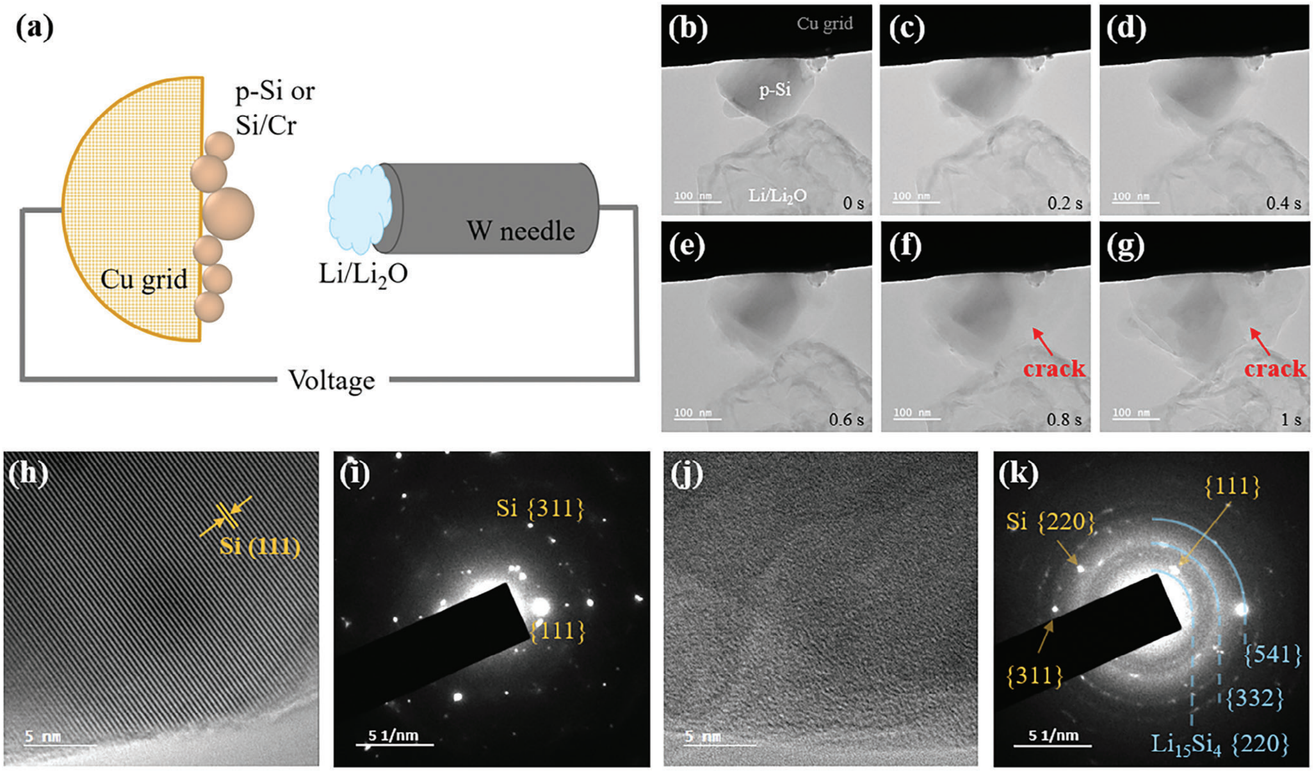

Figure 5. a) Schematic of the setup for in situ TEM lithiation. b–g) Time-resolved TEM images of the lithiation process in the p-Si nanoparticles. HRTEM images and SAED patterns of the h,i) pristine and j,k) lithiated p-Si nanoparticles.

strength,[6] even though the NP is not fully lithiated by the end of the video (Figure 5g). The in situ TEM lithiation video can be seen in the Supporting Information.

HRTEM and SAED patterns were taken for the p-Si NPs before (Figure 5h,i) and after (Figure 5j,k) lithiation. The Si (111) lattice plane with d-spacing of 3.13 Å can be seen in the HRTEM image in Figure 5h. The SAED pattern in Figure 5i shows the Si lattice planes with lattice plane groups {111} and {311}. After lithiation, a large part of the p-Si NP is alloyed into amorphous lithium silicide ($Li_{15}Si_4$). The diffraction of $Li_{15}Si_4$ {220}, {332}, and {541} lattice plane groups can be identified from Figure 5k. It should be noted that a Si core remains at the end of the lithiation (Figure 5g), indicating that the p-Si NP is not fully lithiated by the end of the lithiation process. This can also be confirmed by the diffractions of unlithiated Si {111}, {220}, and {311} lattice plane groups in Figure 5k.

The lithiation process of the Si-8%Cr NPs is shown in **Figure 6**a–f. Compared with the p-Si NPs, the Si-8%Cr NPs are not cracked after full lithiation. The volume of the Si-8%Cr NPs is fully expanded when the Li ions are inserted into the NPs from Figure 5a to f. This shows the 8% Cr content hinders the fracture of Si NPs and improves the structural stability during lithiation. Besides, no crystalline Si core remains after full lithiation, indicating more complete Li diffusion, and higher electronic conductivity by the 8% Cr content. The $CrSi_2$ nanocrystals, as indicated by the green arrows in Figure 6a–f, have low electrochemical reactivity in the lithiation process. The HRTEM images and SAED patterns of the pristine and lithiated Si-8%Cr NPs are shown in Figure 6g,h,i,j, respectively. The pristine Si-8%Cr NPs in Figure 6g show the Si (111) and (220) lattice planes, which can be confirmed by the Si lattice plane groups {111}, {220}, and {311} in the SAED pattern in Figure 6h. The $CrSi_2$ phases with {111} and {112} lattice plane groups can also be identified from the SAED pattern. After lithiation, the crystalline Si is transformed into amorphous $Li_{15}Si_4$, as confirmed by the amorphous $Li_{15}Si_4$ phase in Figure 6i and the SAED pattern in Figure 6j. One of the crystalline $CrSi_2$ nanocrystals, highlighted by the green dashed line in Figure 6i, can be confirmed by the $CrSi_2$ (111) lattice plane, as well as the $CrSi_2$ {111}, {112}, {200}, and {311} lattice plane groups in Figure 6j. The lithiation video of the Si-8%Cr NPs is available in Supporting Information.

The Si-18%Cr NPs were difficult to be lithiated, due to the high doping amount of $CrSi_2$ in the materials. Only one out of four Si-18%Cr NP samples was successfully lithiated by in situ TEM, as shown in Figure S6 (Supporting Information). The volume of Si-18%Cr is increased after lithiation, indicated by the yellow dashed lines in Figure S6a,f (Supporting Information) In the pristine state, both Si (111) and $CrSi_2$ (111) lattice planes can be seen from the HRTEM image in Figure S6g (Supporting Information). The SAED pattern in Figure S6h (Supporting Information) confirms the lattice plane groups of Si {111}, Si {311}, and $CrSi_2$ {111}. Some of the $CrSi_2$ nanocrystals remain in the materials after lithiation, of which the $CrSi_2$ (100) lattice plane can be clearly seen in Figure S6i (Supporting Information). Due to less amount of Si in the Si-18%Cr than the undoped Si or Si-8%Cr, the $Li_{15}Si_4$ phase shows the diffraction of the $Li_{15}Si_4$ lattice plane groups {211}, {220}, {310}, {420}, and {422} with less intensity, as shown in Figure S6j (Supporting Information),

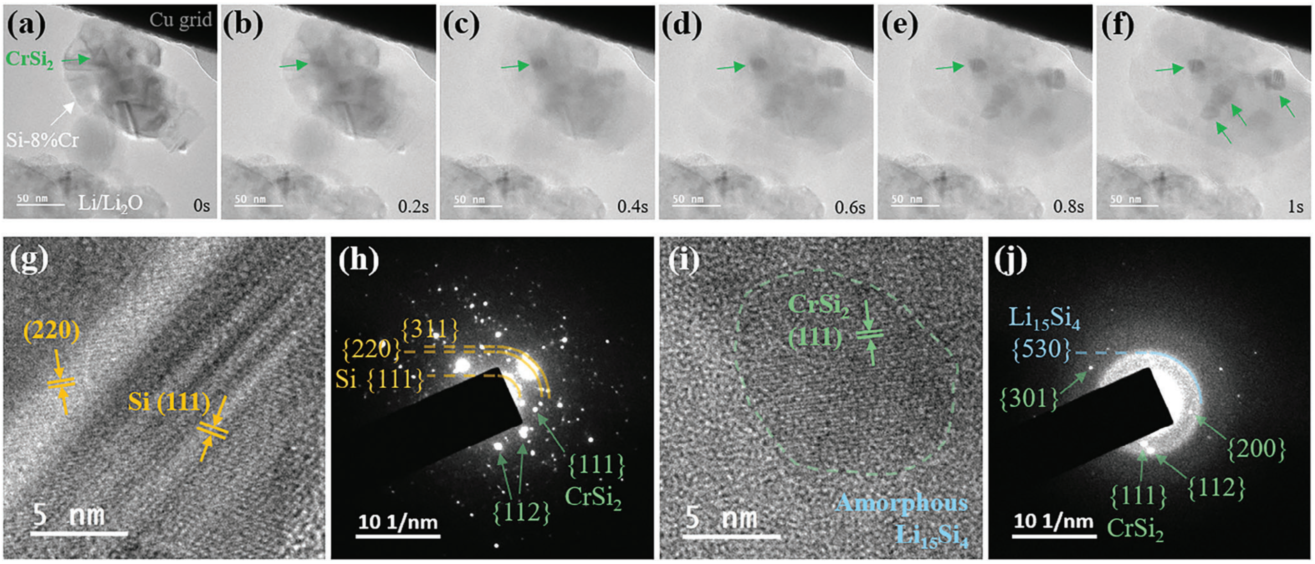

Figure 6. a–f) Time-resolved TEM images showing the lithiation process of the Si-8%Cr nanoparticles. HRTEM images of g) pristine and i) lithiated Si-8%Cr nanoparticles. SAED patterns of h) pristine, and j) lithiated Si-8%Cr nanoparticles.

while the CrSi$_2$ lattice plane {111} can be seen from the SAED pattern.

2.4. Molecular Dynamics Calculation

To shed light on the anti-fracture effect by CrSi2 doping in Si matrix during lithiation, coarse grain molecular dynamics (CGMD) simulations were carried out with the LAMMPS package.[38] **Figure 7a** shows the simulation model, in which the lithiated Si samples have pre-existing crack and then are loaded at a constant tensile strain rate. The L-J force field $U_{LJ}\ (r) = 4\epsilon[(\sigma/r)^{12} - (\sigma/r)^{6}]$ was applied to describe the interactions between the atoms in the system, including the cohesion inside the lithiated Si (Li$_x$Si), the doped Cr (CrSi$_2$), and the interfacial adhesion between Li$_x$Si and CrSi$_2$.

To explain the anti-fracture performance by CrSi$_2$ doping, a quantitative model with physical basis is needed. As shown in Figure 7b,c, we compare the samples of p-Si NP and Si-8%Cr NP with diameter of CrSi$_2$ nanocrystals (D_{CrSi2}) equal to 8 nm, and it can be found that the doped CrSi$_2$ can deflect the crack propagation under a quasi-static tensile loading in the simulation cases. To further verify this finding and overcome the size limitation of the CrSi$_2$ doping, Si-8%Cr NP samples with different D_{CrSi2} are modelled and loaded (see Figure S7a,b, Supporting Information). The CrSi$_2$ nanocrystals with high hardness make the crack swerve, which is a benefit for the anti-fracture performance, compared with the p-Si NPs. The anti-fracture performance of the doped CrSi$_2$ can be quantified by the behavior of the samples under the tensile loading. The stress is normalized by the strength of Li$_x$Si without pre-existing crack, which is shown in Figures S8 and S9 (Supporting Information). The corresponding stress-strain curves and volume of volumetric strain >0.2 in the samples were analyzed. Figure 7d shows the strength (the maximum value of the stress in the samples under tensile loading) increases with the use of CrSi$_2$ doping. In general, the smaller the CrSi$_2$ nanocrystals, the better the anti-fracture performance of the Si/Cr NP anodes. It indicates that during the lithiation process, the doped CrSi$_2$ nanocrystals greatly restrain the crack propagation caused by the volume expansion during lithiation. In Figure 7e, we can see that the volume of volumetric strain >0.2 in the p-Si NP demonstrates a larger distribution along with the pathway of the crack propagation in relative to that of Si-8%Cr NP with $D_{\mathrm{CrSi2}} = 8$ nm, also proving the anti-fracture performance of CrSi$_2$ doping. The volumes of volumetric strain >0.2 part in the Si-8%Cr nanoparticles with $D_{\mathrm{CrSi2}} = 8$, 16, and 32 nm under strain = 7.5% and strain = 10% are smaller than those in the p-Si NP, as shown in Figure 7f. Certainly, for a practical anti-fracture application, such simple patterns (e.g., $D_{\mathrm{CrSi2}} = 8$, 16, and 32 nm) of CrSi$_2$ doping is still at the embryo stage. Its mechanical robustness and the coupling effect in electric field would be the topics of interest for further investigation.

3. Conclusion

In this work, we successfully synthesized and optimized the Si/Cr NP anode materials. With 8% Cr content, the Si NP anode material achieves an extraordinary initial capacity of 1729.3 mAh g^{-1} at 0.2C and maintains 1085 mAh g^{-1} after 500 cycles. At a higher charge rate of 1C, the Si-8%Cr anode material obtain 815.9 mAh g^{-1} after 1000 cycles with a capacity degradation rate of <0.05% per cycle. The excellent cyclability results from the improved structural stability and the enhanced electronic conductivity by CrSi$_2$ doping. In situ TEM lithiation shows that the Si-8%Cr anode material remains the structural integrity during lithiation, and the CrSi$_2$ nanocrystals have low electrochemical reactivity. In addition to the structural stability, the Si-8%Cr NPs can be fully lithiated compared with p-Si and Si-18%Cr NPs, indicating a faster Li diffusion rate, and a higher electronic conductivity by CrSi$_2$ doping. MD simulation shows that CrSi$_2$ nanocrystals in the Si-8%Cr anode material alternate the crack propagation path and therefore increase the overall fracture strength for the

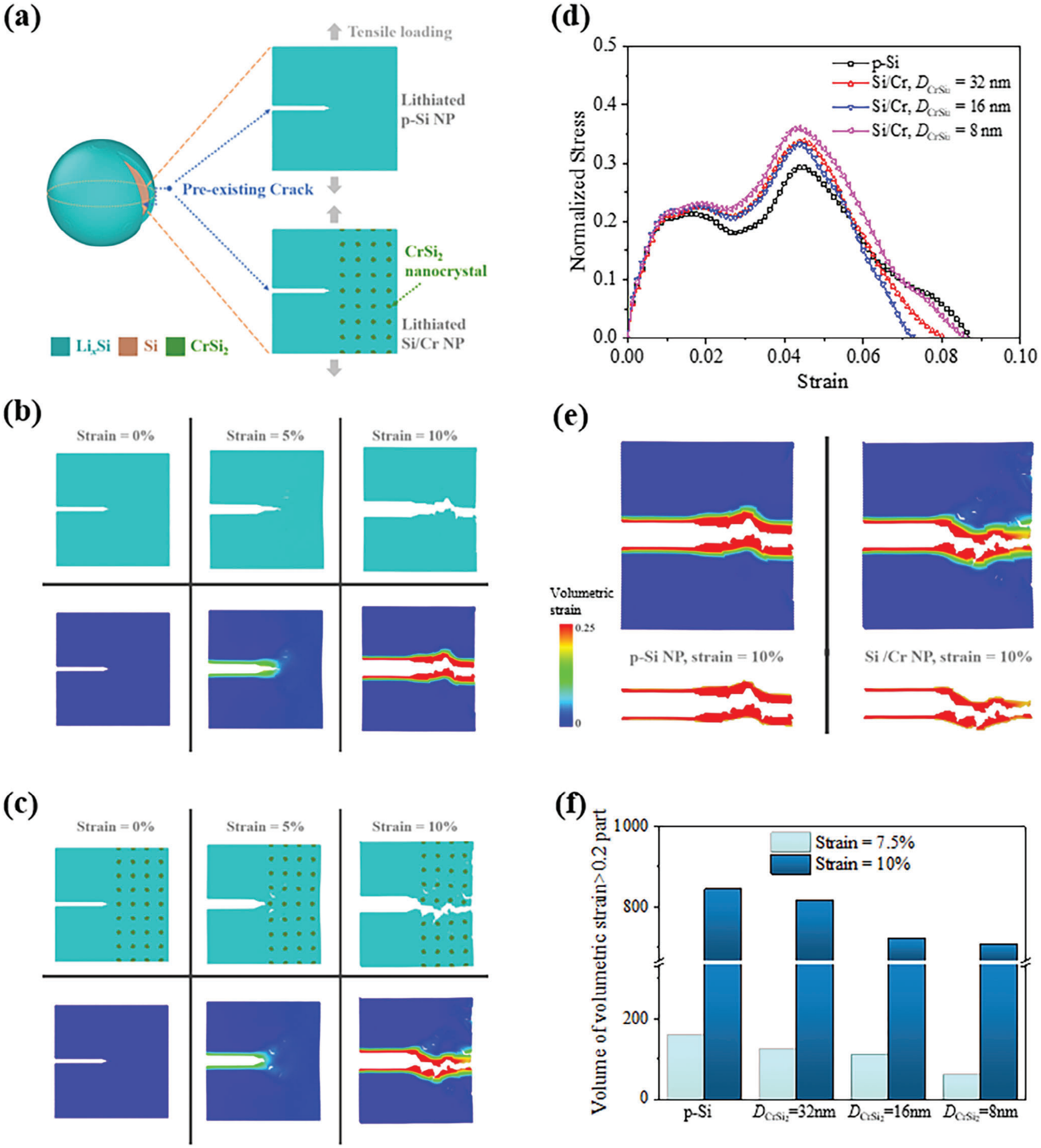

Figure 7. a) Schematic diagram of CGMD simulation of crack propagation in the lithiated p-Si and Si-8%Cr nanoparticles. b) Snapshots of MD simulation and the corresponding strain contour during tensile loading for p-Si nanoparticle. c) Snapshots of MD simulation and the corresponding strain contour during tensile loading for Si-8%Cr nanoparticle with D_{CrSi2} = 8 nm. d) Stress-strain curves of the p-Si nanoparticle and the Si-8%Cr nanoparticles with D_{CrSi2} = 8, 16, and 32 nm. e) Volume of volumetric strain >0.2 part (low figures) in the p-Si nanoparticle and Si-8%Cr nanoparticle with D_{CrSi2} = 8 nm, quantitatively to describe the anti-fracture performance by the CrSi$_2$ nanocrystals in Si matrix. The smaller of the volume, the better of the anti-crack performance. f) Volume of volumetric strain >0.2 part in the p-Si nanoparticle and the Si-8%Cr nanoparticles with D_{CrSi2} = 8, 16, and 32 nm, quantitatively described by using the number of coarse grain units.

Si/Cr anode materials. Therefore, the Si/Cr NP anode is shown to be a promising anode material, which increases charge rate, enhances energy density, and contributes to long cycle life for the next generation LIB.

4. Experimental Section

Materials Synthesis—Synthesis of Chromium Modified Silica: Typically for SiO_2-8%Cr preparation, 1.16 g chromic nitrate ($Cr(NO_3)_3 \cdot 6\ H_2O$, 98%, Aladdin) was dissolved in a mixture of 91 mL ethanol absolute and 9 mL tetraethyl orthosilicate (TEOS, Aladdin, and 98%) under continuous stirring, generating cyaneous solution. After intensively mixed, this solution was injected into another solution of 18 mL ammonia (25 wt%), 32.5 mL ethanol, and 50 ml deionized (DI) water under vigorously stirring. The mixture was stirred continuously for 4 h. All the above procedures were operated under ambient pressure and temperature. The as-prepared blue precipitation was filtrated and washed by ethanol and DI water alternately before drying at 60 °C to acquire the Cr modified SiO_2 precursor. Chromic oxide/silica was marked based on Cr/Si molar ratio as SiO_2-8%Cr (8% Cr), SiO_2-12%Cr (12% Cr), SiO_2-16%Cr (16% Cr), SiO_2-18%Cr (18% Cr), and silica (pure silica).

Materials Synthesis—Synthesis of Silicon: Typically, 1.0 g brown precursor and 10 g NaCl were dissolved in 100 mL DI water. Significantly, the added NaCl was used as heat absorbent during the subsequent magnesiothermic reduction process. The solution was then ultrasonicated for 1 h, followed by water evaporation at 120 °C. After that, SiO_2-8%Cr@NaCl powder and Mg powder were mixed in a mass ratio of Si to Mg being 1:0.85. Then, the mixture was sealed in a Cu reactor in an argon-filled glove box with O_2 content below 0.1 ppm. The reactor was calcined at 700 °C for 6 h in argon (Ar) atmosphere. Afterward, the final product was rinsed with 2.0 M HCl solution to remove the NaCl, MgO, and Mg_2Si, and Si was obtained. Other Si samples were prepared with adjustment of $Cr(NO_3)_3 \cdot 6\ H_2O$ amount during the synthesis of SiO_2. Si samples were marked as Si-8%Cr (from SiO_2-8%Cr), Si-12%Cr (from SiO_2-12%Cr), Si-16%Cr (from SiO_2-16%Cr), Si-18%Cr (from SiO_2-18%Cr), and p-Si (from silica), respectively.

Electrochemical Tests: The electrochemical tests of the above Si anodes were investigated with 2025 type coin cells assembled in an Ar-filled glovebox. The working electrodes were prepared by mixing 60 wt% active materials, 20 wt% SuperP conductive carbon, and 20 wt% sodium alginate binder in DI water. The above slurry was coated on Cu foil. The electrodes were dried in a vacuum oven at 110 °C for 8 h and then cut into films with diameters of 14.0 mm. The mass loading of Si in the electrodes was ≈0.93 ± 0.1 mg cm^{-2}. Lithium (Li) foil, and Celgard 2400 membrane were used as counter electrode and separator, respectively. The liquid electrolyte was composed of 1.0 M $LiPF_6$ in a mixture of ethylene carbonate (EC) and diethyl carbonate (DEC) (1:1, v/v) with 10 wt% FEC additive. Galvanostatic charge/discharge tests were investigated by a CT-2001A LAND battery tester in a voltage window of 1.2 and 0.01 V (vs Li/Li^+). The charge/discharge rates were calculated based on the theoretical capacity of Si (4200 mAh g^{-1}). CV measurement was performed on an electrochemical workstation (P4000, PARSTATMC) at a scan rate of 0.2 mV S^{-1}. EIS was measured with a frequency ranging from 0.01 to 100 kHz.

In Situ TEM Characterization: The synthesized p-Si and Si/Cr NPs were attached on the half-moon Cu grids, as shown in Figure 5a. A small amount of Li metal was scraped from a Li foil to the tip of a W needle inside the Ar-filled glove box. When the holder was transferred from glove box into the TEM (2100 Plus, JEOL) chamber, the surface of Li metal was inevitably oxidized into Li_2O, which served as solid electrolyte for the in situ TEM half cell. After TEM alignment, the Li metal was moved toward the p-Si or Si/Cr NPs. Upon contacting, a larger negative bias (−5 V) than that in a real battery was applied to initiate the lithiation process in the NPs. The whole lithiation process was recorded by a Gatan RIO camera in the TEM. High resolution TEM (HRTEM) images and selected area electron diffraction (SAED) patterns were taken for structural and compositional analysis.

Molecular Dynamics Simulation Model and Simulation Setting Details: Due to the limitation of the computation scale in MD simulation, the size of the sample was taken as 400 nm in length in the simulation system as shown in Figure 7a. The length of pre-existing crack was set as 200 nm. In the Lennard–Jones (L-J) potential describing the cohesion in the lithiated Si, ϵ, and σ were taken as 0.00185 eV and 1.5 nm respectively, giving rise to the effective Young's modulus of the lithiated Si equal to 3.5 GPa;[39] in the L-J potential describing the cohesion in the $CrSi_2$ doping and the interfacial adhesion between the lithiated Si and $CrSi_2$ doping, ϵ and σ were taken as 0.132 eV and 1.5 nm respectively, giving rise to the effective Young's modulus of the $CrSi_2$ doping and interfacial adhesion equal to 250 GPa.[40] In each simulation case, the system was initially relaxed using the canonical ensemble (NVT) for 20000 ps. The time step of the simulations was taken as 100 fs and temperature was controlled at 300 K with the Langevin thermostat. Visualization program OVITO[41] was used to visualize and output the simulations results.

Supporting Information

Supporting Information is available from the Wiley Online Library or from the author.

Acknowledgements

W.L., C.L., and J.F. contributed equally to this work. This work was supported by the UK Faraday Institution (EP/S003053/1) through award FIRG013 "Characterization". Prof. Juan Yang would like to acknowledge the funding (51871247) support from the National Natural Science Foundation of China. Dr. Jimin Fu thanks the support from Start-up Fund for RAPs of HKPolyU (P0043508) and RI-IWEAR Seed Fund of HKPolyU (P0044761).

Conflict of Interest

The authors declare no conflict of interest.

Data Availability Statement

The data that support the findings of this study are available in the supplementary material of this article.

Keywords

$CrSi_2$ doping, crack formation, fast charge, in situ TEM, silicon anode

Received: September 25, 2023
Revised: December 16, 2023

[1] M. T. McDowell, S. W. Lee, W. D. Nix, Y. Cui, *Adv. Mater.* **2013**, *25*, 4966.
[2] S. Chae, S.-H. Choi, N. Kim, J. Sung, J. Cho, *Angew. Chem., Int. Ed.* **2020**, *59*, 110.
[3] Q. Yin, H. Yao, in *Silicon Anode Systems for Lithium-Ion Batteries* (Eds: P. N. Kumta, A. F. Hepp, M. K. Datta, O. I. Velikokhatnyi), Elsevier, Amsterdam, The Netherlands **2022**, Ch.95.
[4] Y. Yan, X. Zhao, H. Dou, J. Wei, W. Zhao, Z. Sun, X. Yang, *Chin. Chem. Lett.* **2021**, *32*, 910.

[5] B. Key, R. Bhattacharyya, M. Morcrette, V. Seznéc, J.-M. Tarascon, C. P. Grey, *J. Am. Chem. Soc.* **2009**, *131*, 9239.
[6] X. H. Liu, L. Zhong, S. Huang, S. X. Mao, T. Zhu, J. Y. Huang, *ACS Nano* **2012**, *6*, 1522.
[7] T. M. Higgins, S.-H. Park, P. J. King, C. (J.) Zhang, N. McEvoy, N. C. Berner, D. Daly, A. Shmeliov, U. Khan, G. Duesberg, V. Nicolosi, J. N. Coleman, *ACS Nano* **2016**, *10*, 3702.
[8] L. Zhang, C. Wang, Y. Dou, N. Cheng, D. Cui, Y. Du, P. Liu, M. Al-Mamun, S. Zhang, H. Zhao, *Angew. Chem., Int. Ed.* **2019**, *58*, 8824.
[9] M. T. McDowell, S. W. Lee, J. T. Harris, B. A. Korgel, C. Wang, W. D. Nix, Y. Cui, *Nano Lett.* **2013**, *13*, 758.
[10] M. Y. Jin, K. Guo, X. Xiao, M. W. Verbrugge, H. Gao, B. W. Sheldon, *Adv. Funct. Mater.* **2021**, *31*, 2010640.
[11] M. Gu, Y. He, J. Zheng, C. Wang, *Nano Energy* **2015**, *17*, 366.
[12] N. Liu, H. Wu, M. T. McDowell, Y. Yao, C. Wang, Y. Cui, *Nano Lett.* **2012**, *12*, 3315.
[13] N. Liu, Z. Lu, J. Zhao, M. T. McDowell, H.-W. Lee, W. Zhao, Y. Cui, *Nat. Nanotechnol.* **2014**, *9*, 187.
[14] J. Tang, Q. Yin, Q. Wang, Q. Li, H. Wang, Z. Xu, H. Yao, J. Yang, X. Zhou, J.-K. Kim, L. Zhou, *Nanoscale* **2019**, *11*, 10984.
[15] C. Wang, H. Wu, Z. Chen, M. T. McDowell, Y. Cui, Z. Bao, *Nat. Chem.* **2013**, *5*, 1042.
[16] W. Li, K. Cao, H. Wang, J. Liu, L. Zhou, H. Yao, *Nanoscale* **2016**, *8*, 5254.
[17] W. Li, Q. Wang, K. Cao, J. Tang, H. Wang, L. Zhou, H. Yao, *Compos. Commun.* **2016**, *1*, 1.
[18] L. Gu, J. Han, M. Chen, W. Zhou, X. Wang, M. Xu, H. Lin, H. Liu, H. Chen, J. Chen, Q. Zhang, X. Han, *Energy Storage Mater.* **2022**, *52*, 547.
[19] S. Dalavi, P. Guduru, B. L. Lucht, *J. Electrochem. Soc.* **2012**, *159*, A642.
[20] K. Schroder, J. Alvarado, T. A. Yersak, J. Li, N. Dudney, L. J. Webb, Y. S. Meng, K. J. Stevenson, *Chem. Mater.* **2015**, *27*, 5531.
[21] S. W. Kim, J. H. Yun, B. Son, Y.-G. Lee, K. M. Kim, Y. M. Lee, K. Y. Cho, *Adv. Mater.* **2014**, *26*, 2977.
[22] Z. Guo, L. Zhou, H. Yao, *Mater. Des.* **2019**, *177*, 107851.
[23] N. Liu, H. Wu, M. T. McDowell, Y. Yao, C. Wang, Y. Cui, *Nano Lett.* **2012**, *12*, 3315.
[24] A. Gohier, B. Laïk, K.-H. Kim, J.-L. Maurice, J.-P. Pereira-Ramos, C. S. Cojocaru, P. T. Van, *Adv. Mater.* **2012**, *24*, 2592.
[25] Q. Xiao, Y. Fan, X. Wang, R. A. Susantyoko, Q. Zhang, *Energy Environ. Sci.* **2014**, *7*, 655.
[26] K. Feng, W. Ahn, G. Lui, H. W. Park, A. G. Kashkooli, G. Jiang, X. Wang, X. Xiao, Z. Chen, *Nano Energy* **2016**, *19*, 187.
[27] H.-Y. Lin, C.-H. Li, D.-Y. Wang, C.-C. Chen, *Nanoscale* **2016**, *8*, 1280.
[28] J. Im, E. K. Jang, S. Kim, S. Yoon, D.-H. Kim, K. Y. Cho, *Chem. Eng. J.* **2020**, *402*, 126292.
[29] X. Zhou, C. Luo, J. Ding, J. Yang, J. Tang, *CrystEngComm* **2020**, *22*, 6574.
[30] F. M. Courtel, D. Duguay, Y. Abu-Lebdeh, I. J. Davidson, *J. Power Sources* **2012**, *202*, 269.
[31] F.-Z. Zhang, Y.-Y. Ma, M.-M. Jiang, W. Luo, J.-P. Yang, *Rare Met.* **2022**, *41*, 1276.
[32] J. Y. Huang, L. Zhong, C. M. Wang, J. P. Sullivan, W. Xu, L. Q. Zhang, S. X. Mao, N. S. Hudak, X. H. Liu, A. Subramanian, H. Fan, L. Qi, A. Kushima, J. Li, *Science* **2010**, *330*, 1515.
[33] M. T. McDowell, I. Ryu, S. W. Lee, C. Wang, W. D. Nix, Y. Cui, *Adv. Mater.* **2012**, *24*, 6034.
[34] M. Gu, Y. Li, X. Li, S. Hu, X. Zhang, W. Xu, S. Thevuthasan, D. R. Baer, J.-G. Zhang, J. Liu, C. Wang, *ACS Nano* **2012**, *6*, 8439.
[35] B. L. Mehdi, J. Qian, E. Nasybulin, C. Park, D. A. Welch, R. Faller, H. Mehta, W. A. Henderson, W. Xu, C. M. Wang, J. E. Evans, J. Liu, J.-G. Zhang, K. T. Mueller, N. D. Browning, *Nano Lett.* **2015**, *15*, 2168.
[36] B. L. Mehdi, A. Stevens, J. Qian, C. Park, W. Xu, W. A. Henderson, J.-G. Zhang, K. T. Mueller, N. D. Browning, *Sci. Rep.* **2016**, *6*, 34267.
[37] Y. Hou, Z. Chen, R. Zhang, H. Cui, Q. Yang, C. Zhi, *Exploration* **2023**, *3*, 20220051.
[38] S. Plimpton, *J. Comput. Phys.* **1995**, *117*, 1.
[39] A. Kushima, J. Y. Huang, J. Li, *ACS Nano* **2012**, *6*, 9425.
[40] R. Gaillac, P. Pullumbi, F.-X. Coudert, *J. Phys.: Condens. Matter* **2016**, *28*, 275201.
[41] A. Stukowski, *Model. Simul. Mater. Sci. Eng.* **2009**, *18*, 15012.